

Actuation manifold from snapshot data

Luigi Marra¹†, Guy Y. Cornejo Maceda², Andrea Meilán-Vila³, Vanesa Guerrero³, Salma Rashwan¹, Bernd R. Noack^{2,4}‡, Stefano Discetti¹, and Andrea Ianiro¹

¹Department of Aerospace Engineering, Universidad Carlos III de Madrid, Av. de la Universidad, 30, Leganés, 28911, Madrid, Spain

²Chair of Artificial Intelligence and Aerodynamics, School of Mechanical Engineering and Automation, Harbin Institute of Technology, 518055 Shenzhen, P. R. China

³Department of Statistics, Universidad Carlos III de Madrid, Calle Madrid, 126, Getafe, 28903, Madrid, Spain

⁴Guangdong Provincial Key Laboratory of Intelligent Morphing Mechanisms and Adaptive Robotics, Harbin Institute of Technology, 518055 Shenzhen, P. R. China

We propose a data-driven methodology to learn a low-dimensional actuation manifold of controlled flows. The starting point is resolving snapshot flow data for a representative ensemble of actuations. Key enablers for the actuation manifold are isometric mapping as encoder and k -nearest neighbour regression as a decoder. This methodology is tested for the fluidic pinball, a cluster of three parallel cylinders perpendicular to the oncoming uniform flow. The centers of these cylinders are the vertices of an equilateral triangle pointing upstream. The flow is manipulated by constant rotation of the cylinders, i.e. described by three actuation parameters. The Reynolds number based on a cylinder diameter is chosen to be 30. The unforced flow yields statistically symmetric unforced periodic shedding represented by a one-dimensional limit cycle. The proposed methodology yields a five-dimensional manifold describing a wide range of dynamics with small representation error. Interestingly, the manifold coordinates automatically unveil physically meaningful parameters. Two of them describe the downstream periodic vortex shedding. The other three ones describe the near-field actuation, i.e. the strength of boat-tailing, the Magnus effect and forward stagnation point. The manifold is shown to be a key enabler for control-oriented flow estimation.

Key words: Flow Control, Low-Dimensional Models, Machine Learning

1. Introduction

In this study, we propose a data-driven manifold learner of the flows for a large range of operating conditions demonstrated by a low-dimensional manifold for the actuated fluidic pinball. A cornerstone of theoretical fluid mechanics is the low-dimensional representation of coherent structures. This representation is a basis for understanding dynamic modeling, sensor-based flow estimation, model-based control and optimization.

Many avenues of reduced-order representations have been proposed. Leonardo da Vinci presented coherent structures and vortices artfully as sketches in a time when the Navier-Stokes equations were not known (Marusic & Broomhall 2021). A quantitative pathway of low-dimensional modeling was started by Hermann von Helmholtz (1858) with his vortex

† Email address for correspondence: luigi.marra@uc3m.es

‡ Email address for correspondence: bernd.noack@hit.edu.cn

laws. Highlights are the von Kármán (1912) model of the vortex street and derivation of feedback wake stabilization from the Föppl’s vortex model by Protas (2004). Orr and Sommerfeld added a stability framework culminating in Stuart’s mean-field theory (Stuart 1958) to incorporate non-linear Reynolds stress effects. The proper orthogonal decomposition (POD) has quickly become the major data-driven approach to compress snapshot data into a low-dimensional Galerkin expansion (Berkooz *et al.* 1993). Cluster-based modeling is an alternative data-driven flow compression, coarse-graining snapshot data into a small set of representative centroids (Kaiser *et al.* 2014). All these low-dimensional flow representations are the kinematic prelude to dynamic models, e.g. point vortex models, modal stability approaches (Theofilis 2011), POD Galerkin models (Holmes *et al.* 2012) and cluster-based network models (Fernex *et al.* 2021).

Data-driven manifold learners are a recent highly promising avenue of reduced-order representations. A two-dimensional manifold may, for instance, accurately resolve transient cylinder wakes: the manifold dimension is a tiny fraction of the order of vortices, POD modes and clusters required for a similar resolution. This manifold may be obtained by mean-field considerations (Noack *et al.* 2003), by dynamic features (Loiseau *et al.* 2018), by locally linear embedding (Noack *et al.* 2023), and by isometric mapping (ISOMAP, Farzamnik *et al.* 2023). In all these approaches, the manifolds have been determined for a single operating condition. Haller *et al.* (2023) emphasized a key challenge, namely it remains “*unclear if these manifolds are robust under parameter changes or under the addition of external, time-dependent forcing*”. This challenge shall be addressed in this study.

We choose the fluidic pinball as our benchmark problem for the proposed manifold learning. This configuration has been proposed by Ishaq *et al.* (2019) as a geometrically simple two-dimensional configuration with a rich dynamic complexity under cylinder actuation and Reynolds number change. The transition scenario is described and modeled by Deng *et al.* (2020) comprising a sequence of bifurcations before passing to chaotic behaviour. The feedback stabilization achieved through cylinder rotation has been accomplished with many different approaches (Raibaudo *et al.* 2020; Cornejo Maceda *et al.* 2021; Li *et al.* 2022; Wang *et al.* 2023). Farzamnik *et al.* (2023) have demonstrated that the unforced dynamics can be described on a low-dimensional manifold.

In this study, we illustrate the development of the control-oriented manifold — called ‘actuation manifold’ in the sequel — for the fluidic pinball with three steady cylinder rotations as independent inputs.

The rest of the manuscript is structured as follows. In §2 we introduce the dataset of the actuated fluidic pinball while in §3 we discuss the methodology employed to distill the actuation manifold and to use it for flow-estimation purposes. The results are presented and discussed in §4, before highlighting the main conclusions of the work in §5.

2. Flow control dataset

The dataset is based on two-dimensional incompressible uniform flow past three cylinders of equal diameter D . Their vertices form an equilateral triangle with one vertex pointing upstream and its median aligned with the streamwise direction. The origin of the Cartesian reference system is located in the midpoint between the two rightmost cylinders. The streamwise and crosswise directions are indicated respectively with x and y . The corresponding velocity components are indicated with u and v . The computational domain Ω is bounded in $[-6, 20] \times [-6, 6]$, and the unstructured grid used has 4225 triangles and 8633 nodes. The data are linearly interpolated on a structured grid with a spacing of 0.05 in both x and y directions.

The Reynolds number (Re), which is based on D and the incoming velocity U_∞ , is set to

30 for all cases. A reference time scale D/U_∞ is set as a convective unit (c.u.). The force coefficients C_L and C_D are obtained by normalizing respectively lift and the drag forces with $\frac{1}{2}\rho U_\infty^2 D$, being ρ the density of the fluid.

The control is achieved with independent cylinder rotations included in the vector $\mathbf{b} = (b_1, b_2, b_3)^T$, with b_1, b_2 and b_3 referring to the front, top, and bottom cylinder tangential speed, respectively. Here, 'T' denotes the transpose operator. Positive actuation values correspond to counter-clockwise rotations. Combinations of rotational speed between -3 and 3 with a step of 1 have been used, for a total of 343 configurations, including the unforced case. The actuations are condensed into a three-parameter vector, that is $\mathbf{p} = (p_1, p_2, p_3)^T$, referred to as Kiki parameters (Lin 2021): boat-tailing $p_1 = (b_3 - b_2)/2$, Magnus effect $p_2 = b_1 + b_2 + b_3$ and forward stagnation point $p_3 = b_1$.

Each simulation is run for 800 c.u. to reach the steady state. Snapshots with 1 c.u. separation in the last 20 c.u. for each steady state have been employed to construct the manifold. The total sampling time is chosen to approximately cover two shedding cycles of the unforced case. This corresponds to a total number of snapshots equal to $M = 6860$.

3. Methodology

The approach proposed here involves employing an encoder-decoder strategy to acquire actuation manifolds, incorporating ISOMAP (Tenenbaum *et al.* 2000) and k -nearest neighbours (k NN) algorithms (Fix & Hodges 1989). The collected dataset undergoes ISOMAP to discern a low-dimensional embedding. Then, the flow reconstruction procedure involves mapping sensors and actuation parameters to the manifold coordinates, followed by interpolation among the k NN to estimate the corresponding snapshot. An overview of this procedure is illustrated in figure 1 and detailed below.

If we consider our flow fields as vector functions $\mathbf{u}(\mathbf{x}) = (u(x, y), v(x, y))$ belonging to a Hilbert space, the inner product between two snapshots \mathbf{u}_i and \mathbf{u}_j is defined by:

$$\langle \mathbf{u}_i, \mathbf{u}_j \rangle = \iint_{\Omega} \mathbf{u}_i(x, y) \cdot \mathbf{u}_j(x, y) dx dy \quad (3.1)$$

where “ \cdot ” refers to the scalar product in the two-dimensional vector space. Norms are canonically defined by $\|\mathbf{u}\| = \sqrt{\langle \mathbf{u}, \mathbf{u} \rangle}$ and distances between snapshots are consistent with this norm.

For our study, we have a collection of M flow field snapshots. In the encoder procedure, the ISOMAP algorithm necessitates determining the square matrix $\mathbf{D}_G \in \mathbb{R}^{M \times M}$ containing the geodesic distances among snapshots. Geodesic distances are approximated by selecting a set of neighbours for each snapshot. Within these neighbourhoods, snapshots are linked by paths whose lengths correspond to Hilbert-space distances. Geodesic distances between non-neighbours are then obtained as the shortest path through neighboring snapshots (Floyd 1962). At this stage, selecting the number of neighbours, which in the encoding part we denote by k_e , is crucial for approximating the geodesic distance matrix. Existing techniques are mostly empirical as in Samko *et al.* (2006). We utilize the less time-consuming approach using the Frobenius norm (denoted by $\|\cdot\|_F$) of the geodesic distance matrix \mathbf{D}_G (Shao & Huang 2005) to determine k_e . Opting for a small k_e can lead to disconnected regions and undefined distances within the dataset, while a large k_e may result in a short-circuiting within the manifold, yielding a Euclidean representation and losing ISOMAP's capability to unfold nonlinear relationships within the dataset.

After constructing the geodesic distance matrix \mathbf{D}_G , multidimensional scaling (Torgerson 1952) is employed to construct the low-dimensional embedding $\mathbf{\Gamma} = (\tilde{\gamma}_{ij})_{1 \leq i \leq M, 1 \leq j \leq n}$. Additionally, the j th column of the matrix $\mathbf{\Gamma}$ is referred to as $\tilde{\gamma}_j$, containing the j th ISOMAP

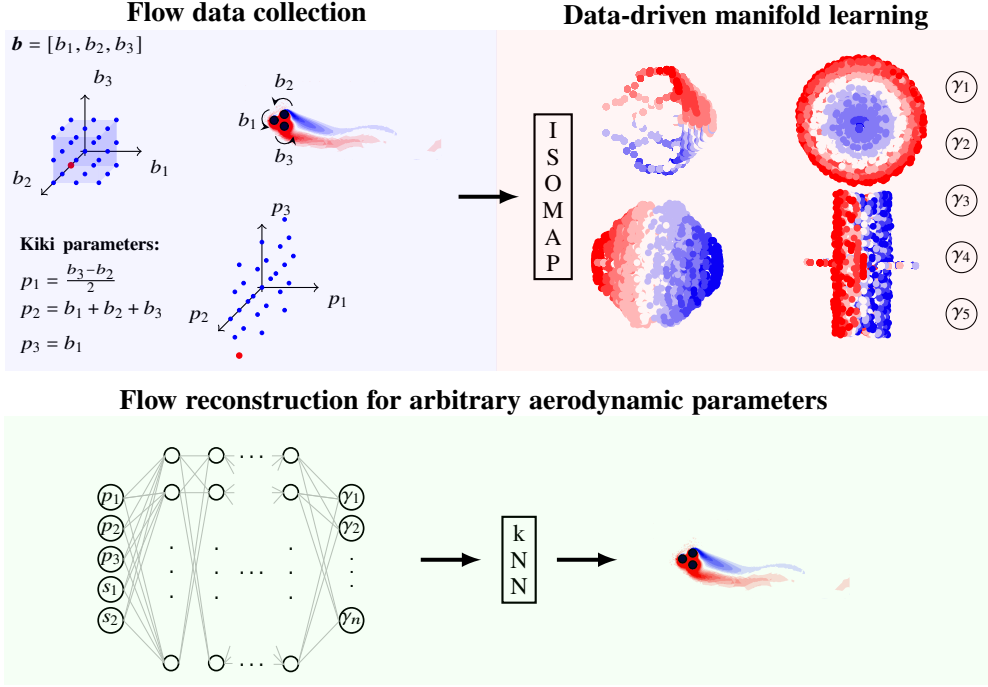


Figure 1: Illustration of the methodology for actuation-manifold learning and full-state estimation. The diagram highlights key steps, from flow data collection to data-driven actuation manifold discovery (upper section). A neural network, incorporating Kiki parameters (p_1 , p_2 and p_3) and sensor information (s_1 and s_2), determines the position in the manifold of a snapshot ($\gamma_1, \gamma_2, \dots, \gamma_n$) and a k NN decoder is used for the full-state flow reconstruction.

coordinate for all the M flow field snapshots and we refer to the ISOMAP coordinates with $\gamma_j, j = 1, \dots, n$.

In this instance, following the methodology outlined by Tenenbaum *et al.* (2000), the evaluation of data representation quality within the ISOMAP technique is conducted through the residual variance $R_v = 1 - R^2(\text{vec}(\mathbf{D}_G), \text{vec}(\mathbf{D}_T))$. Here $R^2(\cdot, \cdot)$ denotes the squared correlation coefficient, 'vec' is the vectorization operator and \mathbf{D}_T represents the matrix containing Euclidean distances in the low-dimensional embedding. The dimension n of the low-dimensional embedding is typically determined by identifying an elbow in the residual variance plot.

After the actuation manifold identification, the objective is to perform a flow reconstruction from the knowledge of a reduced number of sensors and actuation parameters. This process is carried out in two steps. Firstly, a regression model is trained to identify the low-dimensional representation of a snapshot. Specifically, we employ a fully connected multi-layer perceptron (MLP) to map the actuation parameters and sensor information to the manifold coordinates. Secondly, a decoding procedure is conducted through linear interpolation among a fixed number (denoted by k_d) of nearest neighbours, following the methodology established by Farzamnik *et al.* (2023).

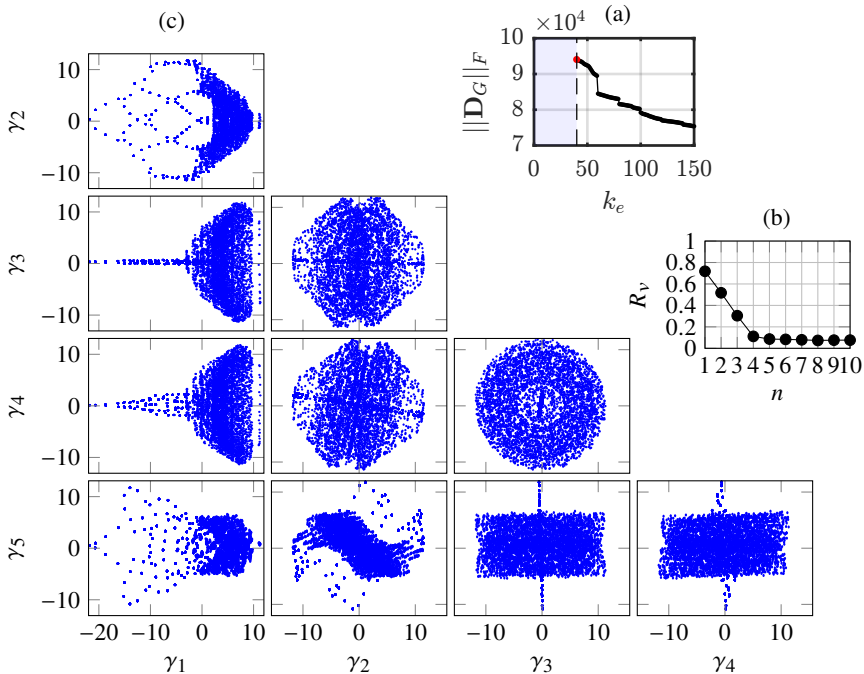


Figure 2: Panel (a) displays the Frobenius norm of the geodesic distance matrix plotted against the number of neighbors employed in Floyd’s algorithm. Results of the manifold obtained for $k_e = 40$ are presented in panels (b) and (c). The former illustrates the residual variance of the first 10 ISOMAP coordinates, while the latter showcases all possible manifold sections identified by the first five coordinates.

4. Results

4.1. Identification and physical interpretation of the low-dimensional embedding

The identified actuation manifold is represented in figure 2. Firstly, the neighbourhood size k_e for the encoding must be determined. The Frobenius norm of the geodesic distance matrix $\|\mathbf{D}_G\|_F$ as a function of k_e is reported in figure 2(a). A minimum $k_e = 40$ is required to ensure that all the neighbourhoods are connected. By increasing it, the Frobenius norm decreases due to improved connections between neighbourhoods. On the other hand, increasing k_e raises the probability of short-circuits, which drastically reduces $\|\mathbf{D}_G\|_F$ (see e.g. $k_e \approx 60$). Choosing a value of k_e within the range from the minimum value up to the point where the first significant drop in $\|\mathbf{D}_G\|_F$ occurs does not result in substantial alterations of the geometry of the manifold or the physical interpretation of its coordinates. Therefore, in this paper, we select the minimum value.

Then the residual variance is used to search for the true dimensionality of the dataset. Employing $n = 5$ coordinates leads to a residual variance of less than 10%, thus $n = 5$ dimensions are deemed sufficient to describe the manifold, as shown in figure 2(b). Further increase in the number of dimensions provides only marginal changes in the residual variance.

The representation of the five-dimensional embedding is undertaken in figure 2(c) in the form of two-dimensional projections on the $\gamma_i - \gamma_j$ planes with $i, j = 1, \dots, 5$ and $i < j$. A first visual observation of the projections highlights interesting physical interpretations. The projection on the $\gamma_3 - \gamma_4$ plane unveils a circular shape, suggesting that these two coordinates describe a periodic feature, i.e. the vortex shedding in the wake of the pinball. The fact that the circle is full suggests that different control actions result in an enhanced or attenuated

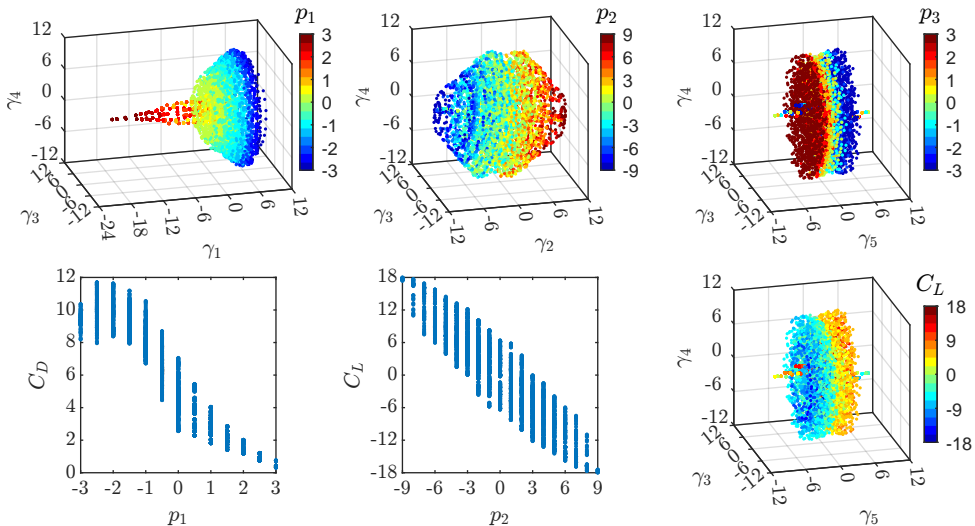


Figure 3: Three-dimensional projections of the manifold color-coded with physical and actuation parameters. The first (boat tailing) and second (Magnus) actuation parameters are plotted against lift and drag coefficients to understand physical control mechanisms.

vortex shedding. Each steady-state describes a circle in the $\gamma_3 - \gamma_4$ plane. The radius of each circle explains the amplitude of vortex shedding, while the angular position provides information about the phase. Cases that do not exhibit vortex shedding collapse into points where $\gamma_3, \gamma_4 \approx 0$. This is evident from the observation of the projections on the planes $\gamma_1 - \gamma_3$ and $\gamma_1 - \gamma_4$, both returning a champagne coupe shape, suggesting that smaller values of γ_1 are a prerogative of the cases with limit cycle of smaller amplitude.

This feature also suggests that γ_1 is correlated with the boat tailing parameter p_1 and thus with the drag coefficient C_D , as visualized in figure 3. This plot also shows a correlation between γ_2 , the Magnus parameter p_2 , and the lift coefficient C_L . The fifth coordinate of the low-dimensional embedding γ_5 , on the other hand, appears to be correlated with the stagnation point parameter p_3 and partially explains the lift produced by the pinball. Intriguingly, all ISOMAP coordinates are physically meaningful and allow us to discover the three Kiki parameters without human input.

Another interesting physical interpretation arises observing the manifold section $\gamma_1 - \gamma_2$. This provides insights into the horizontal symmetry of the data. In the figure, semicircles repeat, increasing in number as γ_1 increases. Within each of them, b_1 varies from -3 to 3 , while b_2 and b_3 remain fixed. The branches symmetrically positioned with respect to the axis $\gamma_2 = 0$ are associated with symmetric actuation b_2 and b_3 .

The low-dimensional embedding, being the result of the eigenvector decomposition of the double-centered squared-geodesic distance matrix, is made of orthogonal vectors. While this might represent a disadvantage to other autoencoders (Otto & Rowley 2022), this also allows projecting the snapshots on this basis and obtaining spatial modes that can be used to corroborate the physical interpretation of the manifold coordinates. The j th spatial mode ϕ_j , $j = 1, \dots, n$ is a linear combination of the snapshots \mathbf{u}_i , i.e. $\|\tilde{\gamma}_j\| \phi_j = \sum_{i=1}^M \tilde{\gamma}_{ij} \mathbf{u}_i$.

The first five ISOMAP modes are visualized in figure 4 with a line integral convolution (LIC, Forssell & Cohen 1995) plot superimposed on a velocity magnitude contour plot. The visual observation of the modes confirms the interpretation of the physical meaning of the coordinates of the low-dimensional embedding. Three modes, namely ϕ_1 , ϕ_2 , and ϕ_5 are representative of the actuation parameters. The first ISOMAP mode is characterized by

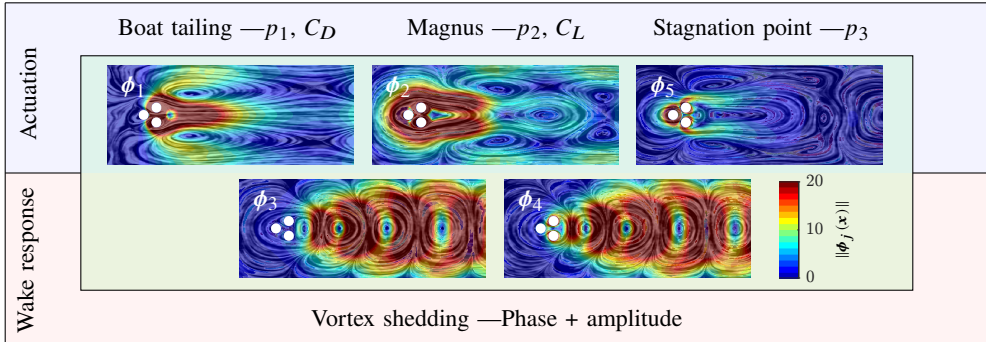


Figure 4: LIC representations of the normalized actuation modes. The shadowed contour represents the local velocity magnitude of the pseudomodes.

Input layer size	5	Output layer size	5
Number of samples	6860	Loss	mean-square-error
Training set	90%	Batch size	2048
Validation set	10%	Number of epochs	Early stop on validation loss
Test set	22 external cases	Optimizer	Adam
I/O scaling	Mean-std \rightarrow [0, 1]	Activation function	tanh
Hidden layers MLP ₁	(70,70,70,70)	Hidden layers MLP ₂	(40,40)

Table 1: Structure of the neural networks used for latent coordinate identification.

the presence of a jet (wake) downstream of the pinball due to boat tailing (base bleeding). The second ISOMAP mode represents a circulating motion around the pinball, responsible of positive or negative lift, depending on the circulation direction. The fifth mode is characterized by a net circulation around the front cylinder, determining the position of the front cylinder stagnation point, if added to the mean field. The two spatial modes ϕ_3 and ϕ_4 , instead, have the classical aspect of vortex shedding modes. Together, they describe the wake response to actuation parameters (far field), providing information on the intensity and phase of vortex shedding.

4.2. Flow estimation

For the identification of the position of a flow field snapshot within the manifold, we employ a fully connected multi-layer perceptron. The mapping is done having as inputs a limited number of sensors and the Kiki parameters. The latter provides comprehensive knowledge of the coordinates representing the near field (γ_1 , γ_2 , and γ_5). Far-field coordinates (γ_3 and γ_4) identification is helped by having sensors providing information on the intensity and phase of vortex shedding. Two different alternatives are proposed here. In the first, we utilize the lift coefficient and its one-quarter mean shedding period delay (we refer to this case with MLP₁). In the second, crosswise components of velocity are measured at two positions in the wake, specifically at points $\mathbf{x}_1 = (8, 1)$ and $\mathbf{x}_2 = (10, 1)$ (MLP₂). The characteristics of the employed networks are summarized in table 1. The training of the neural networks is performed with the dataset used to construct the data-driven manifold randomly removing all snapshots related to 10% of the actuation cases and using the remaining ones for validation.

To test the accuracy of flow estimation, we use 22 additional simulations with randomly-selected actuation parameters, not present in the training nor the validation dataset. As done

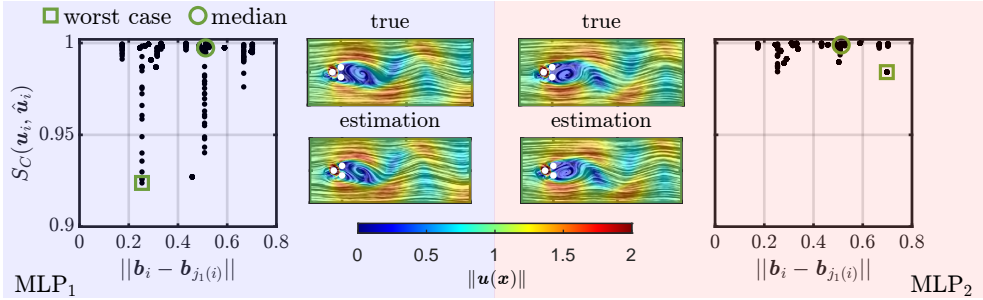


Figure 5: Cosine similarity between real and reconstructed snapshots for all 22 actuation cases in the test dataset. Reconstruction error is plotted against the distance of each actuation case (\mathbf{b}_i) to its nearest neighbor in the training dataset $\mathbf{b}_{j_1(i)}$. In the center, a comparison between the true snapshot and its estimation is presented for the median error case. Figure presented with LIC and color-coded by velocity magnitude. The number of neighbours is fixed to $k_d = 200$. Results are shown for MLP_1 (left) and MLP_2 (right).

for the training dataset, the last 20 c.u. are sampled every 1 c.u. for a total of 440 snapshots. The neural networks are used to identify the positions of these cases within the low-dimensional embedding and then the k NN decoder is applied to reconstruct the full state. In the decoding phase, we select $k_d = 200$ neighboring points to minimize the full state reconstruction error through a brute force approach on the validation dataset. A reason why this parameter is significantly higher than the k_e for the encoding part resides in the fact that for some control actions, the vortex shedding in the wake is removed. This causes the snapshots related to these cases to collapse into one single position in the physical and the low-dimensional space (since γ_3 and γ_4 are approximately 0). Around these snapshots, a small number of neighbours would cause issues in the linear interpolation of the k NN decoding. One solution to this problem would be replacing the 20 steady case with a single snapshot for each actuation. However, this approach is discarded to minimize user intervention in the method.

The accuracy of the estimation between the true (\mathbf{u}_i) and estimated ($\hat{\mathbf{u}}_i$) snapshots is quantified in terms of cosine similarity $S_G(\mathbf{u}_i, \hat{\mathbf{u}}_i) = \langle \mathbf{u}_i, \hat{\mathbf{u}}_i \rangle / (\|\mathbf{u}_i\| \|\hat{\mathbf{u}}_i\|)$. Results can be observed in figure 5, the knowledge of the manifold enables a full state estimation with few sensors and minimal reconstruction error. When performing the flow reconstruction using MLP_1 , the median cosine similarity is 0.9973, corresponding to a median root-mean-square error (RMSE) of 0.0559. Using MLP_2 , instead, the median cosine similarity is 0.9989 (RMSE = 0.0357).

5. Conclusions

In this study, we address a challenge of reduced-order modeling: accurate low-dimensional representations for a large range of operating conditions. The flow data is compressed in a manifold using ISOMAP as encoder and k NN as decoder. The methodology is demonstrated for the fluidic pinball as an established benchmark problem of modeling and control. The cylinder rotations are used as three independent steady control parameters. Starting point of the reduced-order modeling is a data set with 20 statistically representative post-transient snapshots at $Re = 30$ for 343 sets of cylinder rotations covering uniformly a box with circumferential velocities between -3 and 3 .

The ISOMAP manifold describes all snapshots with 5 latent variables and few percent representation error. To the best of our knowledge, this is the first demonstration of data-driven manifold learning for a flow under multiple input control. Intriguingly, all latent variables are aligned with clear physical meanings. Three coordinates correspond to near-field actuation

effects. More precisely, these coordinates are strongly aligned with the Kiki parameters \mathbf{p} introduced by Lin (2021), describing (i) the level of boat tailing (base bleeding) p_1 leading to drag reduction (increase), (ii) the strength of the Magnus effect p_2 leading to a steady lift and characterizing (iii) the forward stagnation point p_3 . Two further coordinates correspond to the wake response to actuation, i.e. the amplitude and phase of vortex shedding. The distillation of physically meaningful parameters from a fully automated manifold is surprising and inspiring (see figure 1).

Our low-rank model is a key enabler for flow estimation with a minimum number of sensors. It is possible to estimate the full flow state with small reconstruction errors just by knowing the actuation parameters and employing two additional measurements, namely the aerodynamic forces or the flow velocity in two points of the wake.

We emphasize that the low-dimensional characterization of post-transient dynamics as a function of three actuation constitutes a modeling challenge and encourages numerous further applications, e.g. vortex-induced vibration of a cylinder at different spring stiffnesses and cylinder masses, aerodynamic flutter of an elastic airfoil with different wing elasticities, combustion instabilities for different reaction parameters, just to name a few. A low-dimensional manifold representation can be utilized for understanding, estimation, prediction, and model-based control. Summarizing, the presented results can be expected to inspire a large range of applications and complementary manifold learning methods.

Acknowledgements. We thank Qixin ‘Kiki’ Lin for laying the groundwork of this study with her pioneering master thesis.

Funding. This work is supported by the National Science Foundation of China (NSFC) through grants 12172109, 12172111 and 12302293, by the Guangdong Basic and Applied Basic Research Foundation under grant 2022A1515011492, by the Guangdong Provincial Key Laboratory of Intelligent Morphing Mechanisms and Adaptive Robotics, by the Shenzhen Science and Technology Program under grant JCYJ20220531095605012, by the projects PITUFLOW-CM-UC3M and PREDATOR-CM-UC3M, funded by the call “Estímulo a la Investigación de Jóvenes Doctores/as” within the frame of the Convenio Plurianual CM-UC3M and the V PRICIT (V Regional Plan for Scientific Research and Technological Innovation) and by the project ARTURO, ref. PID2019- 109717RB-I00/AEI/10.13039/501100011033, funded by the Spanish State Research Agency.

Declaration of interests. The authors report no conflict of interest.

Data availability statement. All codes and datasets will be made openly available upon publication of the manuscript.

Author ORCIDs. L. Marra, <https://orcid.org/0000-0001-9422-2808>; G. Y. Cornejo Maceda <http://orcid.org/0000-0001-7499-7569>; A. Meilán-Vila, <https://orcid.org/0000-0001-8537-9280>; V. Guerrero, <https://orcid.org/0000-0002-6610-7455>; B. R. Noack, <https://orcid.org/0000-0001-5935-1962>; S. Discetti, <https://orcid.org/0000-0001-9025-1505>; A. Ianiro, <https://orcid.org/0000-0001-7342-4814>.

REFERENCES

- BERKOOZ, G., HOLMES, P. & LUMLEY, J. L. 1993 The proper orthogonal decomposition in the analysis of turbulent flows. *Annu. Rev. Fluid Mech.* **25** (1), 539–575.
- CORNEJO MACEDA, G. Y., LI, Y., LUSSEYRAN, F., MORZYŃSKI, M. & NOACK, B. R. 2021 Stabilization of the fluidic pinball with gradient-enriched machine learning control. *J. Fluid Mech.* **917**, A42.
- DENG, N., NOACK, B. R., MORZYŃSKI, M. & PASTUR, L. R. 2020 Low-order model for successive bifurcations of the fluidic pinball. *J. Fluid Mech.* **884**, A37.
- FARZAMNIK, E., IANIRO, A., DISCETTI, S., DENG, N., OBERLEITHNER, K., NOACK, B. R. & GUERRERO, V. 2023 From snapshots to manifolds – a tale of shear flows. *J. Fluid Mech.* **955**, A34.
- FERNEX, D., NOACK, B. R. & SEMAAN, R. 2021 Cluster-based network modeling—From snapshots to complex dynamical systems. *Sci. Adv.* **7** (25), eabf5006.
- FIX, E. & HODGES, J. L. 1989 Discriminatory analysis. nonparametric discrimination: Consistency properties. *Int. Stat. Rev.* **57** (3), 238–247.

- FLOYD, R. W. 1962 Algorithm 97: Shortest path. *Commun. ACM* **5** (6), 345.
- FORSSELL, L. K. & COHEN, S. D. 1995 Using line integral convolution for flow visualization: Curvilinear grids, variable-speed animation, and unsteady flows. *IEEE T. Vis. Comput. Gr.* **1** (2), 133–141.
- HALLER, G., KASZÁS, B., LIU, A. & AXÅS, J. 2023 Nonlinear model reduction to fractional and mixed-mode spectral submanifolds. *Chaos* **33** (6), 063138.
- HELMHOLTZ, H. 1858 Über integrale der hydrodynamischen gleichungen, welche den wirbelbewegungen entsprechen. *J. Reine Angew. Math.* **55**, 25–55.
- HOLMES, P., LUMLEY, J. L., BERKOOZ, G. & ROWLEY, C. W. 2012 *Turbulence, Coherent Structures, Dynamical Systems and Symmetry*. Cambridge University Press.
- ISHAR, R., KAISER, E., MORZYŃSKI, M., FERNEX, D., SEMAAN, R., ALBERS, M., MEYSONNAT, P. S., SCHRÖDER, W. & NOACK, B. R. 2019 Metric for attractor overlap. *J. Fluid Mech.* **874**, 720–755.
- KAISER, E., NOACK, B. R., CORDIER, L., SPOHN, A., SEGOND, M., ABEL, M., DAVILLER, G., ÖSTH, J., KRAJNOVIĆ, S. & NIVEN, R. K. 2014 Cluster-based reduced-order modelling of a mixing layer. *J. Fluid Mech.* **754**, 365–414.
- VON KÁRMÁN, T. 1912 Über den Mechanismus des Widerstandes, den ein bewegter Körper in einer Flüssigkeit erfährt. *Nachrichten von der Gesellschaft der Wissenschaften zu Göttingen, Mathematisch-Physikalische Klasse* **1912**, 547–556.
- LI, Y., CUI, W., JIA, Q., LI, Q., YANG, Z., MORZYŃSKI, M. & NOACK, B. R. 2022 Explorative gradient method for active drag reduction of the fluidic pinball and slanted ahmed body. *J. Fluid Mech.* **932**, A7:1–48.
- LIN, Q. 2021 Fully automated control-oriented reduced-order modeling exemplified for the fluidic pinball. Master’s thesis, Harbin Institute of Technology.
- LOISEAU, J.-CH., NOACK, B. R. & BRUNTON, S. L. 2018 Sparse reduced-order modeling: Sensor-based dynamics to full-state estimation. *J. Fluid Mech.* **844**, 459–490.
- MARUSIC, I. & BROOMHALL, S. 2021 Leonardo da Vinci and fluid mechanics. *Annu. Rev. Fluid Mech.* **53**, 1–25.
- NOACK, B. R., AFANASIEV, K., MORZYŃSKI, M., TADMOR, G. & THIELE, F. 2003 A hierarchy of low-dimensional models for the transient and post-transient cylinder wake. *J. Fluid Mech.* **497**, 335–363.
- NOACK, B. R., EHLERT, A., NAYERI, C. N. & MORZYŃSKI, M. 2023 Analysis, modeling, and control of the cylinder wake. In *Data-Driven Fluid Mechanics: Combining First Principles and Machine Learning* (ed. M. A. Mendez, A. Ianiro, B. R. Noack & S. L. Brunton), pp. 3–19. Cambridge University Press.
- OTTO, S. E. & ROWLEY, C. W. 2022 Inadequacy of linear methods for minimal sensor placement and feature selection in nonlinear systems: A new approach using secants. *J. Nonlinear Sci.* **32** (5), 69.
- PROTAS, B. 2004 Linear feedback stabilization of laminar vortex shedding based on a point vortex model. *Phys. Fluids* **16** (12), 4473–4488.
- RAIBAUDDO, C., ZHONG, P., NOACK, B. R. & MARTINUZZI, R. J. 2020 Machine learning strategies applied to the control of a fluidic pinball. *Phys. Fluids* **32**, 015108:1–13.
- SAMKO, O., MARSHALL, A.D. & ROSIN, P.L. 2006 Selection of the optimal parameter value for the isomap algorithm. *Pattern Recognit. Lett.* **27** (9), 968–979.
- SHAO, C. & HUANG, H. 2005 Selection of the optimal parameter value for the isomap algorithm. In *MICAI 2005: Advances in Artificial Intelligence* (ed. Alexander Gelbukh, Álvaro de Albornoz & Hugo Terashima-Marín), pp. 396–404. Springer Berlin Heidelberg.
- STUART, J. T. 1958 On the non-linear mechanics of hydrodynamic stability. *J. Fluid Mech.* **4** (1), 1–21.
- TENENBAUM, J. B., DE SILVA, V. & LANGFORD, J. C. 2000 A global geometric framework for nonlinear dimensionality reduction. *Science* **290** (5500), 2319–2323.
- THEOFILIS, V. 2011 Global linear instability. *Annu. Rev. Fluid Mech.* **43**, 319–352.
- TORGERSON, W. S. 1952 Multidimensional scaling: I. Theory and method. *Psychometrika* **17** (4), 401–419.
- WANG, X., DENG, N., CORNEJO MACEDA, G. Y. & NOACK, B. R. 2023 Cluster-based control for net drag reduction of the fluidic pinball. *Phys. Fluids* **35** (2).